

# Confinement in fibrous environments positions and orients mitotic spindles

Apurba Sarkar <sup>a,†</sup>, Aniket Jana <sup>b,†</sup>, Atharva Agashe <sup>b,†</sup>, Ji Wang<sup>c</sup>, Rakesh Kapania <sup>d</sup>, Nir S. Gov <sup>e</sup>, Jennifer G. DeLuca <sup>f</sup>, Raja Paul <sup>a,\*</sup> and Amrinder S. Nain <sup>b,c,\*</sup>

<sup>a</sup>School of Mathematical and Computational Sciences, Indian Association for the Cultivation of Science, Jadavpur, Kolkata 700032, India

<sup>b</sup>Department of Mechanical Engineering, Virginia Tech, Blacksburg, VA 24061, USA

<sup>c</sup>Department of Biomedical Engineering and Mechanics, Virginia Tech, Blacksburg, VA 24061, USA

<sup>d</sup>Department of Aerospace and Ocean Engineering, Virginia Tech, Blacksburg, VA 24061, USA

<sup>e</sup>Department of Chemical and Biological Physics, Weizmann Institute of Science, Rehovot 7610001, Israel

<sup>f</sup>Department of Biochemistry and Molecular Biology, Colorado State University, Fort Collins, CO 80523, USA

\*To whom correspondence should be addressed: Email: [raja.paul@iacs.res.in](mailto:raja.paul@iacs.res.in) (R.P.); Email: [nain@vt.edu](mailto:nain@vt.edu) (A.S.N.)

<sup>†</sup>A.S., A.J., and A.A. contributed equally to this work.

Edited By Dennis Discher

## Abstract

Accurate positioning of the mitotic spindle within the rounded cell body is critical to physiological maintenance. Mitotic cells encounter confinement from neighboring cells or the extracellular matrix (ECM), which can cause rotation of mitotic spindles and tilting of the metaphase plate (MP). To understand the effect of confinement on mitosis by fibers (ECM confinement), we use flexible ECM-mimicking nanofibers that allow natural rounding of the cell body while confining it to differing levels. Rounded mitotic bodies are anchored in place by actin retraction fibers (RFs) originating from adhesions on fibers. We discover that the extent of confinement influences RF organization in 3D, forming triangular and band-like patterns on the cell cortex under low and high confinement, respectively. Our mechanistic analysis reveals that the patterning of RFs on the cell cortex is the primary driver of the MP rotation. A stochastic Monte Carlo simulation of the centrosome, chromosome, membrane interactions, and 3D arrangement of RFs recovers MP tilting trends observed experimentally. Under high ECM confinement, the fibers can mechanically pinch the cortex, causing the MP to have localized deformations at contact sites with fibers. Interestingly, high ECM confinement leads to low and high MP tilts, which we mechanistically show to depend upon the extent of cortical deformation, RF patterning, and MP position. We identify that cortical deformation and RFs work in tandem to limit MP tilt, while asymmetric positioning of MP leads to high tilts. Overall, we provide fundamental insights into how mitosis may proceed in ECM-confining microenvironments in vivo.

## Significance Statement

Mitosis proceeds with the cell body rounding up, during which it encounters confinement from neighboring tissue, influencing mitotic spindle organization. Confinement outcomes are unknown for isolated cells interacting with a few extracellular matrix fibers. Using flexible and suspended fibers that mimic native architectures, we detail confinement effects as mitotic bodies push against the fibers. Confined rounded bodies are anchored in position by actin retraction fibers, whose 3D patterning on the cell cortex depends upon confinement levels. While 2D methods impose artificial confinement to achieve metaphase plate (MP) rotations through improper rounding, we show that natural and full rounding of cell bodies in fiber networks can also have MP rotations, thus distinguishing confinement biology on fibers from extensive studies in 2D.

## Introduction

Eukaryotic cell division proceeds with interphase cells undergoing significant shape changes to become rounded cell bodies. The stiff cortex of spherical cells is held in place by two dominant mechanical cues: retraction fibers (RFs) and mechanical confinement (1–5). Actin-rich RFs connect the cell body with sites of interphase adhesions, thus acting as stabilizing mechanical links for proper positioning of the mitotic spindle (1, 6–8). The level of RF coverage

in fibrous environments leads to diverse mitotic outcomes and errors (9). On the other hand, confinement from the neighboring cells is “volumetric” and can happen without RFs (10, 11). Improper rounding under confinement can lead to mitotic spindle orientation defects, increased mitotic errors, delayed or halted division, and even cell death (4, 11–17). In loose connective tissues and interstitial matrices having sparse organization of fibrillar collagens (18–24), it is conceivable that rounded mitotic cells are

**Competing Interest:** The authors declare no competing interests.

**Received:** April 30, 2025. **Accepted:** June 3, 2025

© The Author(s) 2025. Published by Oxford University Press on behalf of National Academy of Sciences. This is an Open Access article distributed under the terms of the Creative Commons Attribution-NonCommercial License (<https://creativecommons.org/licenses/by-nc/4.0/>), which permits non-commercial re-use, distribution, and reproduction in any medium, provided the original work is properly cited. For commercial re-use, please contact reprints@oup.com for reprints and translation rights for reprints. All other permissions can be obtained through our RightsLink service via the Permissions link on the article page on our site—for further information please contact journals.permissions@oup.com.

held in place by RFs while also mechanically confined between the extracellular matrix (ECM) fibers (we define this to be ECM confinement). Recent intravital *in vivo* imaging of breast cancer cells has shown cells migrating along aligned collagen fibers, exerting forces through protrusions that cause fiber deformations and rounded cells confined between two parallel fibers (25). Here, we inquire about the combined action of these cues (RFs and ECM confinement) to direct mitotic spindle positioning and orientation.

The position and orientation of the mitotic spindle within cells dictate the division axis, crucially determining symmetric or asymmetric cell division, thereby impacting cell fate, tissue development, and homeostasis (26–29). Improper spindle orientation can have significant physiological consequences (30, 31). Recent work by Tan et al. (32) highlights that an off-centered metaphase plate (MP) promotes asymmetric divisions with unequal daughter cell sizes, while a centrally aligned MP supports symmetric cell divisions. In epithelial tissues, spindle orientation parallel to the tissue plane ensures symmetric division, allowing daughter cells to spread within the tissue plane and contributing to tissue elongation and development (28, 33, 34). Conversely, apicobasal spindle orientation supports asymmetric division in epithelial cells and promotes tissue stratification, as seen in mouse skin development and the terminal end buds of mammary ducts (35, 36). In cultured cells on fibronectin micropatterns, external forces transmitted through RFs orient the spindle along these cues, potentially promoting symmetric cell divisions (1, 3, 6). Therefore, proper spindle orientation within the tissue and RF cues are crucial for proper organ development and maintaining tissue homeostasis. Spindle misorientation is often associated with developmental disorders, including microcephaly, cancer, defects in tissue architecture, and cell fate misspecification (30, 31, 37). Thus, understanding the mechanisms regulating spindle orientation is essential for ensuring proper tissue development, growth, and disease prevention.

Numerous strategies have been developed to study the individual contributions of RFs and confinement on mitosis. RFs are part of the cortical mechanosensory complex, which links the cell cortex to the astral microtubules to transmit the effects of external cues to organize the mitotic spindle (6, 38). Our prior work has shown that increased RF coverage on the cell cortex with increasing density of underlying ECM-mimicking nanofibers limits rounded cell body movement, causing faster division and a higher incidence of multipolar defects (9). Studies using flat tissue culture plates and fibronectin-coated micropatterns have shown that RFs formed on the coverslips promote spindle alignment parallel to the substrate (1, 2). On the other hand, when sandwiching (confining) cells between two fibronectin-coated coverslips, the spindles are oriented perpendicularly to the substrate due to the influence of RFs generated on both the bottom and top coverslips (7). Volumetric confinement using an atomic force microscope (AFM) cantilever placed directly on the rounded cell has shown that low confining forces (~5 nN) accelerate mitotic progression, while at larger confining forces (~100 nN), the integrity of the mitotic spindle and the overall mitotic progression is impaired (4, 5). Maintaining proper orientation of mitotic spindles under confinement requires appropriate tension levels at intercellular junctions in the epithelium plane (33, 39), but increasing the confining forces by using dense gels leads to delayed division (10), buckling of mitotic spindles (40), and spindle multipolarity defects leading to cell death (14).

Here, we introduce a repeatable system of ECM-mimicking suspended nanofibers capable of interrogating the combined effects of ECM confinement and RFs in orienting the mitotic spindle. The suspended and flexible nature of fibers allows the natural

rounding of cells undergoing division, confining them to differing levels while mechanically linking the cortex and interphase adhesion sites through RFs. We find that the extent of confinement regulates the 3D patterning of RFs on the cortex, and high confinement causes localized deformations of the cell cortex and, consequently, in the MP. For a mechanistic interpretation of the outcome due to the combined effects of cortical deformation and RF patterning, we developed a stochastic Monte Carlo *in silico* framework accounting for the centrosome (CS), chromosome (CH), and membrane interactions. We discover that the patterning of RFs primarily regulates the MP tilt, and the cortical pinching creates physical constraints on MP positioning and complements the RFs under high ECM confinement to reduce the MP tilt. Overall, we provide knowledge of the combined effects of ECM confinement and RF patterning in orienting the mitotic spindle, as conceivably expected in fibrous *in vivo* environments.

## Results

### Mechanical confinement in fiber networks enables measurement of mitotic forces and induces tilt of the MP

Mitotic cells exert outward forces as they round up against volumetric confinement. In our previous work, we showed that cells attached to two fibers (12  $\mu\text{m}$  apart) underwent division by balling up while being held by RFs originating from four adhesion sites on fibers (Fig. 1a(i), [Movies S1](#) and [S2](#)) (9). Often, the cells got trapped between the two fibers, causing them to bow outwards (Fig. 1a(i), [Movies S2](#) and [S3](#)), which we termed as ECM confinement. Naturally, we inquired if our model system could be used to study the combined effects of the extent of confinement and RF arrangement on orienting the mitotic spindle and MP. To quantify the extent of confinement, we analyzed the basal-apical positioning of the rounded cell with respect to the fiber plane from the confocal cross-sectional side views ( $yz$ , Fig. 1a(ii)). We measured two heights: cell height ( $H$ ) and height of fiber plane ( $h$ ) from the bottom of the cell, with a value of  $h/H=0$ , indicating a pure unconfined cell positioned on top of fibers (no bowing out of fibers), and  $h/H=0.5$  showing confinement at the cell mid-plane with the maximum outward bulge of fibers and formation of two cellular lobes. Thus, we categorized cells as confined for  $h/H$  values ranging from 0.3 to 0.5 and unconfined for  $h/H$  ratios ranging from 0 to 0.3 (Fig. 1a(iii)). Mechanical confinement resulted in noticeable cortical deformations at sites of contact with fibers (yellow arrowheads in Fig. 1a), which was associated with increased cell height (Figs. 1a(iv) and [S1a](#)) and aspect ratio (Fig. [S1b](#)).

The bending of fibers allowed us to estimate the forces during interphase, mitosis, and post-cell division (Fig. 1b(i, ii), [Movie S4](#)) using Nanonet Force Microscopy ([Appendix I in Supplementary Material](#)) (41–43). During interphase, cells are in their natural contractile state and thus deflect the fibers inward (pink arrows, Fig. 1b(i, ii)). Contractile forces are, by convention, considered to be positive. Following mitotic entry in confined conditions, cells progressively round up by forcing the fibers outwards (yellow arrows, Fig. 1b(i, ii)). Consistent with literature-reported data, we observed a steady increase in the magnitude of the rounding forces from nuclear envelope breakdown, with peak mitotic forces of ~12–14 nN achieved during metaphase (5, 44). In contrast, in the case of unconfined cells, we did not observe appreciable expansive forces (outward deflection of fibers). Since RFs anchored the cells, our force measurement platform allowed us to estimate the tension in RFs. We estimated the tension in RFs (~214 pN) by assuming RFs from each adhesion site to be analogous to

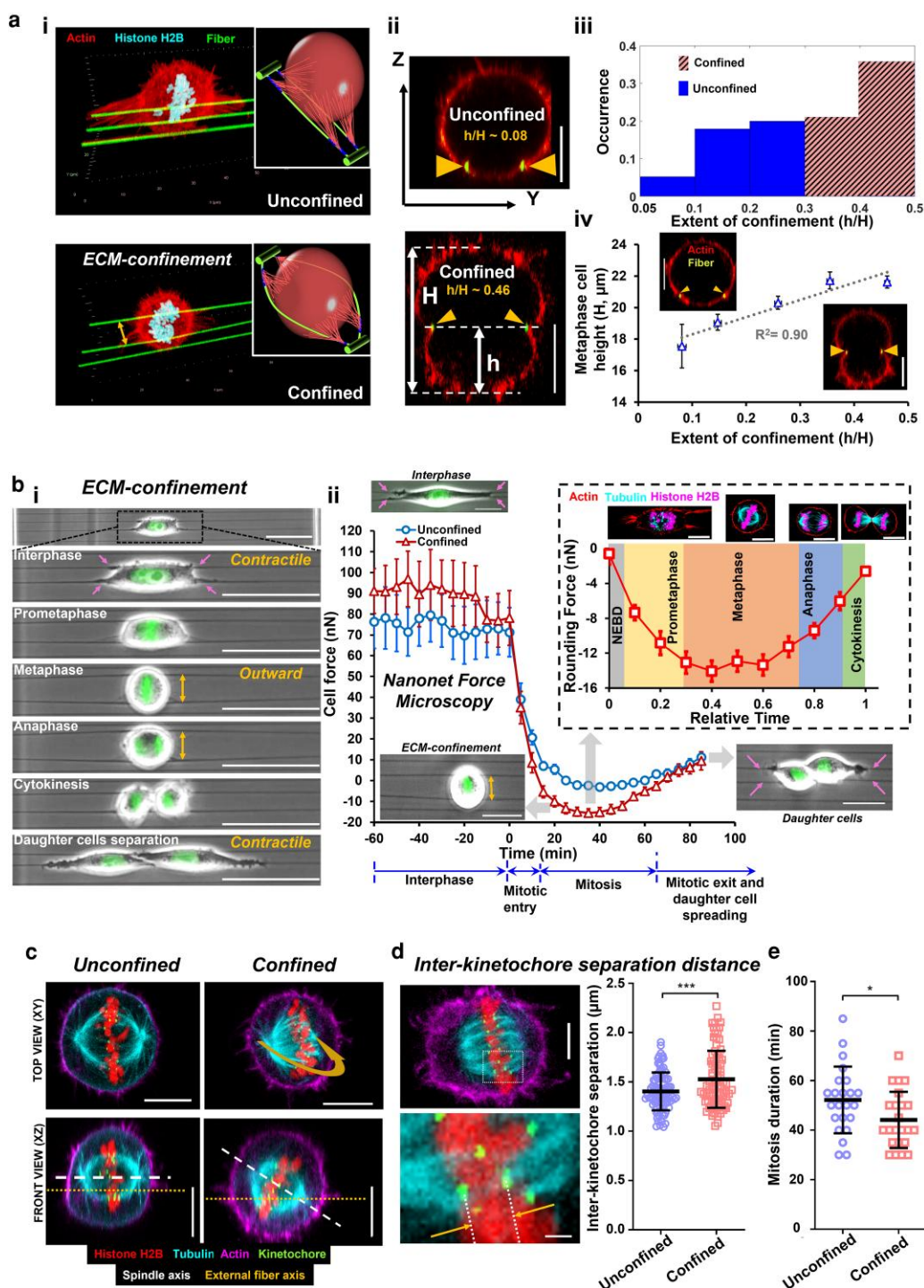


**Fig. 1.** Mechanical confinement of mitotic cells in fibrous environments. **a**) (i) Representative 3D isometric views of single fixed mitotic cells on top of fibers (unconfined) or trapped between two fibers (confined), actin (cell cortex), histone H2B (CHs) and the fibers (fibronectin coating) are indicated in red, cyan, and green respectively. Inset cartoons highlight the outward bowing of fibers during ECM confinement. (ii) Representative side views ( $yz$  cross-section) of fixed unconfined and confined cells with the fibers as green dots (yellow arrowheads).  $H$  represents the cell height taken at metaphase, and  $h$  is the height from the fiber plane to the bottom of the cell. Scale bars are  $10 \mu\text{m}$ . (iii) Histogram showing relative occurrence of the different levels of confinement (quantified by  $h/H$ ,  $N = 10$ ,  $n = 73$ ). (iv) Metaphase cell height increases with confinement ( $h/H$ ) ( $R^2 = 0.9$ ,  $P = 0.0132$ ;  $N = 10$ ,  $n = 73$ ). Representative cross-sectional images of fixed mitotic cells with very low  $h/H$  ( $\sim 0.1$ ) and high  $h/H$  ( $\sim 0.5$ ). Scale bars are  $10 \mu\text{m}$ . **b**) (i) Time-lapse images of a representative live mitotic confined cell undergoing cell division. (ii) Nanonet Force Microscopy–based force profiles of confined and unconfined cells transitioning from interphase to mitosis, with inset images showing a live single cell at different stages. By convention, mitosis forces are shown as negative to represent outward deflection of fibers. The dashed rectangle box shows the average force profiles for confined cells rounding during mitosis which is normalized for time taken from NEBD to cytokinesis ( $N = 4$ ,  $n = 23$ ) along with representative top views of fixed cells undergoing various stages of division. Scale bars are (i)  $50 \mu\text{m}$  and (ii)  $20 \mu\text{m}$ . **c**) Representative top ( $xy$ ) and front ( $xz$ ) views of fixed, confined and unconfined cells demonstrating the 3D tilt of the MP. The yellow arrow represents the MP rotation. Cells are stained with actin cortex (magenta), microtubules (cyan), KTs (green), and CHs (red). Scale bars represent  $10 \mu\text{m}$ . **d**) Representative fixed images showing the measurement of inter-KT separation and the quantitation showing an increase in the average inter-KT distance with confinement. Scale bars represent  $5 \mu\text{m}$ . **e**) Confinement causes a drop in the mitosis duration,  $N = 5$ ,  $n = 47$ .

springs-in-parallel (average number of RFs  $\sim 10$  per focal adhesion cluster, Fig. S2). Following the mitotic exit, we observed that daughter cells started spreading and re-applying contractile forces (Fig. 1b(ii)).

Next, we investigated whether the ECM confinement affected the organization of the mitotic spindle and MP. We found that ECM confinement caused the mitotic spindles to rotate inside the cell body with a large MP tilt visualized from the xz front views of confocal z-stack images (Fig. 1c). Additionally, ECM confinement correlated with an increase in the average inter-kinetochore (KT) separation distance during metaphase (Fig. 1d) and significantly faster mitosis (Fig. 1e). The observation that increased inter-KT separation distance corresponds to faster mitotic durations aligns with our previous observations on cells placed in different fibrous environments (9), demonstrating that increased inter-KT separation with an increasing density of underlying ECM fibers correlates with faster mitotic exit. Cytokinesis events captured from live cell imaging revealed substantial reorientation of the cell division axis under ECM confinement (Fig. S3 and Movie S5).

Overall, we quantified the mitotic forces as cells balled up under ECM confinement. We found that ECM confinement caused tilting of the MP and reduced mitotic durations.

## The patterning of RFs governs MP tilting

We wanted to interrogate the factors responsible for the tilt of the MP under ECM confinement. We identified two key parameters: (i) the extent of mechanical confinement and (ii) the 3D organization of the RFs. Using confocal microscopy, we generated 3D z-stacks of fluorescently labeled fibers, cell cortex, and the MP (Fig. 2a(i, ii)) and analyzed cells with well-defined flat-disk-shaped MPs from the maximum intensity projection in the yz side view, which enabled us to measure the MP tilt from the xz front view (see cartoon inset in Fig. 2a(iii)). We found a strong correlation between average MP tilt from the xz front views and the extent of confinement from yz side views ( $R^2 = 0.96$ , Fig. 2a(iii)). MP tilt in the xy top view showed a marginal increase under high confinement (Fig. S4). We focused exclusively on front-view measurements for their stronger correlation with confinement ( $h/H$ ). Instances of complete 3D MP rotation, which prevented MP tilt measurements, were excluded from our analysis (Fig. S5).

Next, we analyzed the spatial patterning of RFs under different levels of ECM confinement. From the xy top views, we observed that both confined and unconfined cells were held in space by four sets of RFs attaching the cell cortex region between the external fibers (top view in Fig. 2a(i, ii)). Such an arrangement originates from the adhesion geometry of these cells during interphase, which agrees with our previous study (9). We observed that the patterning of RFs extended from the fiber plane to the cells' mid-cortical (equatorial) level (Fig. S6). To quantify ECM confinement-driven RF coverage, we measured the proportion of the cortical perimeter (xz-view) covered by RFs (Fig. 2b(i)). We found RF coverage decreased with increasing levels of confinement ( $h/H$ , Fig. 2b(ii)), signifying a band- and triangle-like pattern of RFs at high and low confinement, respectively (Fig. 2b(ii, inset) and c(i)).

Next, we sought to mechanistically explain the underlying mechanisms causing the variation in the MP tilt as a function of the extent of confinement ( $h/H$ ) and the RF patterns. We developed a computational model to account for CSs, CHs, KT, and cell cortex in a rounded mitotic cell. The model is built upon our earlier framework (9, 45), with augmentation to include spatial organization of experimentally observed RF patterns during ECM confinement. We simulated a pairwise interaction model where

the model entities (CSs, CHs, and KT) interacted among themselves and with the cell cortex through forces that vary with the separation distance (45–48). However, the forces between CS and KT are assumed to be distance independent (45, 49). Thus, our model includes five fundamental forces: CS attraction to each other, CS attraction to the KT, CS repulsion from the CH arms, and short-range attraction among CSs to the RF regions and the remaining cortex (CRTX) (Fig. 2c(ii) and details of the model are included in Appendix II in Supplementary Material). These forces arise from microtubule dynamics and molecular motors interacting with various model components (48). The CS–CS, CS–CH, and CS–KT forces were maintained at a base value corresponding to a bipolar majority (45). The interaction forces between CSs and RFs transmitted through the astral MTs were set several times stronger than those from the remaining CRTX (see Table SII for model parameters). This choice of force parameters is consistent with our earlier observation that the RFs interact with the CSs  $\sim 4$  to 10 times stronger than the remaining CRTX. Such consideration is crucial for achieving the observed propensity of spindle statistics in cells undergoing mitosis in various fibrous environments (9). Coupling the five force interactions in a stochastic energy minimization framework, we performed Monte Carlo simulations to achieve stable mechanical equilibria of the spindle.

Next, we computationally investigated the mechanism behind the MP tilt under ECM confinement. Our experiments showed that the extent of confinement correlated with changes in cell height and patterning of RFs in band like and triangular shapes at high and low confinement, respectively. We recreated the RF patterns in our model (Fig. 2c(i); see simulated RF pattern in Table SI, Case 4). We determined that the contribution of cell height to MP tilting was insignificant (Fig. S7). Our computational model successfully reproduced the observed trend of increased MP tilt with increasing levels of confinement (Fig. 2c(iii)). The model suggests that the smaller MP tilts at low ECM confinement result from the increased RF coverage (Fig. 2b(ii)) due to the triangle-like patterning of the RFs. Experimental estimates of RF coverage from (xz) front views of the cells (Fig. 2b(ii)) correlate with the RF coverage area (area of cell cortex regions covered by the RFs) in our simulations (Fig. S8). As the RF adhesion pattern on the cell cortex changes with confinement, from triangular patterns at low ECM confinement to band-like patterns at high ECM confinement, the RF coverage area decreases accordingly. The increased RF coverage area at low ECM confinement causes a substantial pull on the CSs from the RF regions, yielding lower MP tilt. Maintaining similar RF coverage by expanding the band-like RF pattern at high confinement to match the maximum RF coverage of the triangular pattern at low confinement leads to a decrease in MP tilt at high confinement compared with low confinement, contradicting experimental observations (Fig. S9). We simulated various configurations to determine whether RF arrangements other than the experimentally observed triangular pattern at low ECM confinement can also produce the observed trend of MP tilt (Table SI). Notably, deviations like rectangular RF spots or band-like patterns extending from the fiber plane to the cell equator, despite following a similar trend of RF coverage area with confinement, failed to replicate the experimental MP tilt trend across varying confinement levels ( $h/H$ ; see columns 3 and 4 in Table SI). Therefore, by combining experiments and mechanistic computational modeling, we demonstrate the area and geometric patterning of RFs (triangular shape in unconfined and band like in confined) influence MP tilting.

Although the average tilt angle increases with  $h/H$ , polar histograms of MP tilts from our simulations at low ( $h/H \sim 0.1$ ) and high

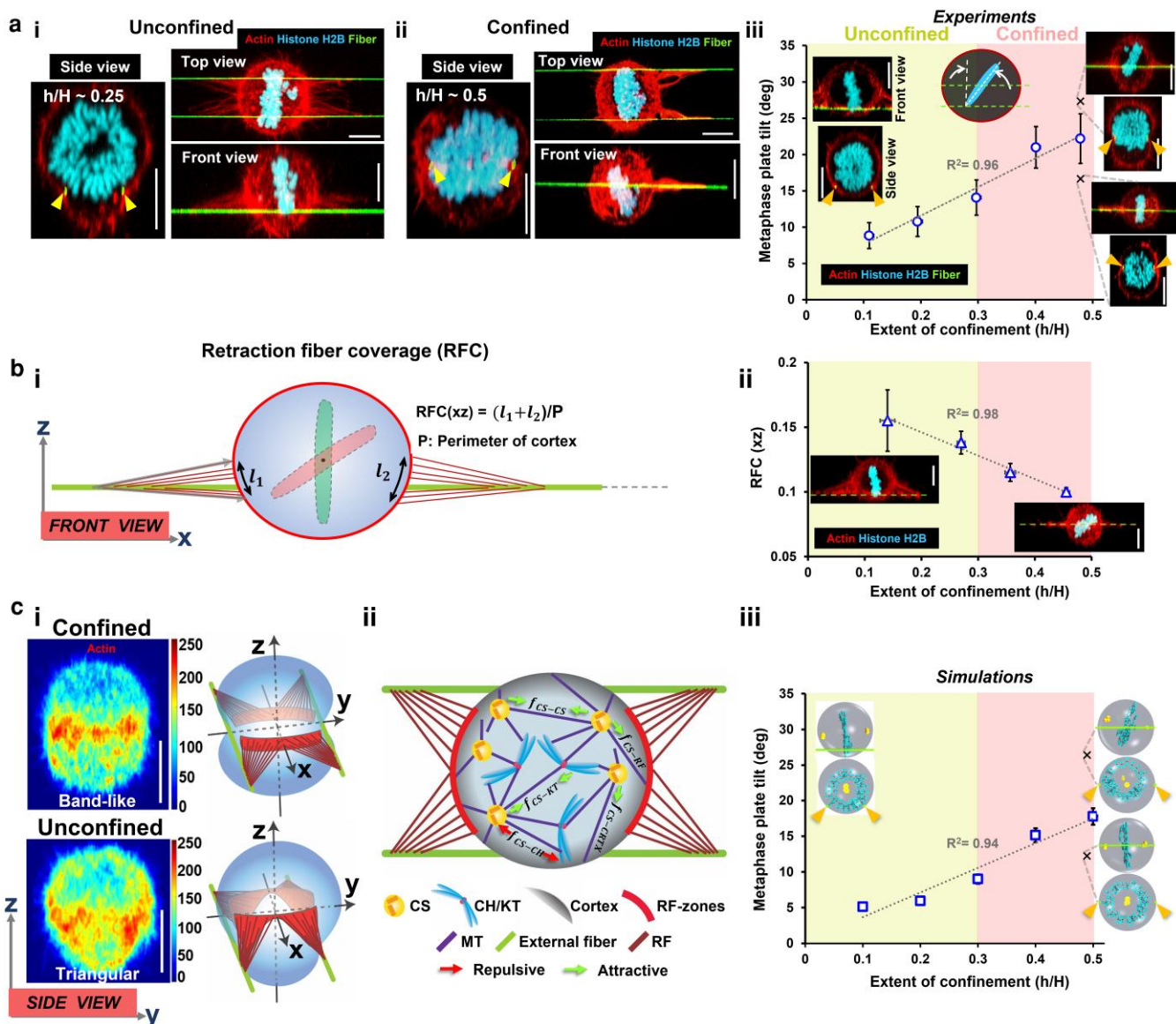


**Fig. 2.** Computational modeling recapitulate experimentally observed MP tilt with increasing confinement. **a** (i, ii) Representative images of fixed unconfined and confined cells with top ( $xy$ ), side ( $yz$ ), and front ( $xz$ ) views shown, actin, histone H2B, and fibronectin are shown in red, cyan, and green to identify the cell cortex, MP, and the fibers, respectively. Scale bars are  $10\ \mu\text{m}$ . (iii) MP tilt as a function of the extent of confinement ( $h/H$ ). Inset images show front and side views of fixed unconfined ( $h/H \sim 0.1$ ) and confined ( $h/H \sim 0.5$ ) cells. The angle is measured from a normal drawn to the fiber axis (green dashed lines shown for confined and unconfined cases) ( $N = 10$ ,  $n = 73$ ). Scale bars are  $10\ \mu\text{m}$ . **b** (i) Schematic showing the quantification of the RF coverage. (ii) RF coverage decreases with  $h/H$ . Inset images showing RF organization in representative front views of fixed, confined and unconfined cells. Scale bars are  $10\ \mu\text{m}$  ( $N = 5$ ,  $n = 44$ ). **c** (i) Intensity heat map demonstrating the average projection of  $yz$  side views in actin-stained cells. Scale bars are  $10\ \mu\text{m}$ . Band-like arrangement emerges for RF organization in confined cells, while unconfined cells have triangular forms of RF regions that extends downwards from the mid-cortical level, corresponding adopted RF regions for the computational simulations. (ii) Computational model of the mitotic cell between the two external fibers (marked in green). CSs attract each other ( $f_{CS-CS}$ ) or KTJs ( $f_{CS-KT}$ ) and are attracted to the cortex region devoid of RFs ( $f_{CS-CRTX}$ ) or coupled to RFs ( $f_{CS-RF}$ ). CSs repel CH arms ( $f_{CS-CH}$ ). All relevant components of the mitotic machinery are marked and indexed below.  $f_{CS-RF}$  attraction is considered several times stronger than  $f_{CS-CRTX}$ . (iii) Computational data for MP tilt as a function of  $h/H$  without cortex deformation, representative snapshots showing the front and side views of spherical unconfined and confined cells. Average MP tilt is estimated from  $\sim 500$  simulations with different random initializations for each condition. Error bars represent the SEM measured with respect to the corresponding mean values of the data. Note that crosses in **a**(iii) and **c**(iii) show the low and high MP tilt angles observed at high confinement along with representative images. The average of these two angles is plotted in the main figure, and the origin of two configurations is explained in Fig. 3.

ECM confinement ( $h/H \sim 0.5$ ) show distinct distributions (Fig. S10). In low confinement, most MPs are positioned within a narrow angular width. In contrast, cells under high ECM confinement exhibit  $\sim 60\%$  of MPs at low angles ( $\leq 10^\circ$ ), with the remainder displaying a broader distribution, which leads to a larger average MP tilt at high ECM confinement. Next, we investigate the factors contributing to both high and low tilts under high ECM confinement (shown by crosses in Fig. 2a(iii) and c(iii)) and what limits MP tilts.

### The interplay of RFs and cortical pinching regulates the extent of MP positioning and tilt under high ECM confinement

Next, we inquired about the origin of low and high MP tilt angles at high ECM confinement ( $h/H \sim 0.5$ ). We found that high confinement by the parallel fibers could pinch the cell, forming two symmetric cellular lobes due to local deformation in the cortex. Thus, we interrogated the independent contributions of cortical

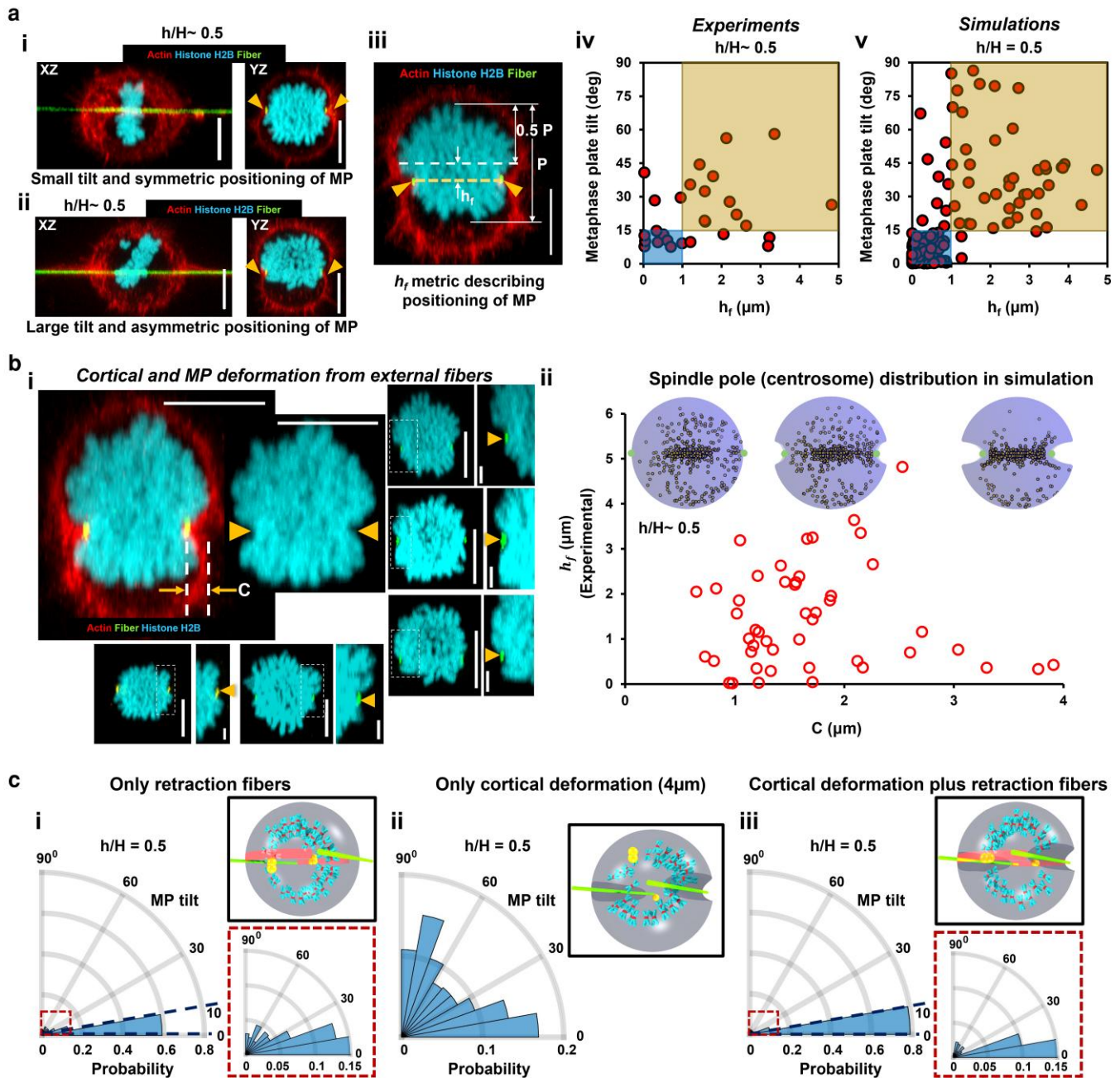


**Fig. 3.** Relative influence of pinching and RF distribution on the MP tilt angle in confined cells. **a** (i, ii) Front (xz) and side (yz) views of representative fixed, confined cells with similar confinement level ( $h/H \sim 0.5$ ) but with small and large MP tilt respectively. (iii) Representative side view of a confined cell showing the  $h_f$  metric, which denotes the distance between the center of the MP and the plane of the fibers. “P” denotes the length of MP, and  $0.5 P$  defines the MP mid-plane. (iv, v) MP tilt angles as a function of  $h_f$  obtained from both experiments ( $N = 6$ ,  $n = 28$ ) and computational modeling (from 200 independent simulations). Blue- and yellow-shaded regions represent low  $h_f$  ( $\leq 1 \mu\text{m}$ ) associated with low MP tilts ( $\leq 15^\circ$ ) and high  $h_f$  ( $> 1 \mu\text{m}$ ) associated with high tilt angles ( $> 15^\circ$ ), respectively. **b** (i) Side view of a representative fixed, confined cell demonstrating the cortical deformations (C) induced by the external fibers. C is measured as the horizontal distance from the fiber position to the line tangent to the cortical surface of the cell. Inset demonstrates that cortical deformations can further lead to deformations (denoted by yellow triangles) within the MP. Five more representative cases showing deformations in the cortex and MP, with scale bars of  $2 \mu\text{m}$  in magnified views of boxed regions. (ii) Plot of  $h_f$  as a function of cortical deformation (C) from experiments ( $N = 5$ ,  $n = 48$ ). The insets show scatter plots of spindle pole (CS pole) positions for different deformations ( $C = 0, 2$ , and  $4 \mu\text{m}$ ) from 500 independent simulations per C, visualized from side views of the cells. For clarity, only the spindle pole located in the front half of the cell (from the side view) is displayed. **c** Polar histograms of the MP tilt angles generated from  $\sim 500$  independent simulations in the presence of (i) only RFs, (ii) only cortical deformation (with  $C = 4 \mu\text{m}$ ), and (iii) the presence of both cortical deformations ( $C = 4 \mu\text{m}$ ) and RFs. Insets in (i) and (iii) demonstrate a magnified view of the polar histograms. CSs are in yellow, CHs are in blue, KTs are in red, and two green lines denote external fibers. RF attachment areas are represented as two light red bands on the cell surface. All scale bars represent  $10 \mu\text{m}$ , unless noted.

pinching and RFs in tilting the MP under high ECM confinement. A close examination of the confocal front (xz) and side (yz) views revealed the MP plate to be symmetrically (similar proportion in both cellular lobes) and asymmetrically (major proportion in

one cellular lobe) positioned (Fig. 3a(i, ii)). We developed a new metric  $h_f$  (Fig. 3a(iii)), denoting the distance between the MP centroid and the fiber plane to describe the proportion of MP in cellular lobes: a value closer to zero signifying equal proportion in both

lobes. From our experiments and simulations, we observed a higher occurrence of cells with low  $h_f$  ( $<1\ \mu\text{m}$ ) that were associated with lower MP tilt angles ( $\leq 15^\circ$ ; Figs. 3a(iv, v) and S11). However, for  $h_f$  values  $>1\ \mu\text{m}$  (MP positioned asymmetrically), we predominantly observed higher MP tilt angles ( $>15^\circ$ ; Fig. 3a(iv, v)). Inspection of confocal images of  $h_f >1\ \mu\text{m}$  cases revealed one of the spindle poles was positioned far from the RF regions. In contrast, the other pole remained close to the band-like RF regions on the opposite cell side [see Fig. 1c (confined case front view) and Fig. S12].

Next, our confocal images revealed large deformations at sites of pinching of the cortex by external fibers (Fig. 3b(i)). We probed the extent of deformation from outside the cell cortex ( $C$  in Fig. 3b(i)) and found a measurable  $C$  ( $>1\ \mu\text{m}$ ) only at high confinement ( $h/H \sim 0.4\text{--}0.5$ ). Contrary to intuition, we found no correlation between  $C$  and  $h/H$  (Fig. S13). We believe that variations in cortex stiffness and cell sizes may cause an imbalance between the outward forces from the rounding cell and the compression from external fibers, leading to different degrees of deformation at the same confinement level. We found that these deformations led to sharp changes in MP at sites of pinching from the external fibers (Fig. 3b(i) with more representative examples), suggesting a probable physical limitation in the translation of MP. On the other hand, unconfined cells, with fibers far below the equatorial plane experiencing minimal outward forces, showed negligible cortical and MP deformation (Fig. S14). To determine whether cortical deformation imposes geometric constraints on CS/CH movement, we examined how MP position ( $h_f$ ) varied with cortical deformation ( $C$ ) in our experiments (Fig. 3b(ii)). While smaller deformations showed no clear correlation, larger deformations were associated with lower  $h_f$  values. Given the limited number of experimental cases with significant deformation, we turned to simulations for further insight. We plotted the spindle pole (centrosomal pole) distribution from the side view in simulations. We found that spindle poles were positioned closer to the fiber plane at large cortical deformations (Fig. 3b(ii), insets). Spindle poles near the RF region at the cell mid-cortical level correspond to spindle alignment parallel to the fiber plane, with low MP tilt and low  $h_f$ , whereas a scattered spindle pole from the RF region reflects a misaligned spindle with a large MP tilt and large  $h_f$ . Direct estimation of  $h_f$  from simulations confirmed that more significant cortical deformation ( $C > 2\ \mu\text{m}$ ) correlated with  $h_f < 1\ \mu\text{m}$  (Fig. S15a). Incidentally, confinement caused a significant drop in MP fluctuations from the xy top views (Fig. S16), likely due to different RF arrangements in confined versus unconfined cells and cortical deformation at high confinement.

Next, we used our computational framework to examine the cooperative ability of cortical deformation and RFs to regulate the MP tilting under high ECM confinement. First, we examined the effect of RFs by themselves, followed by the combined impact of RFs and cortical deformation. In the absence of cortical deformation, RFs were able to align almost 60% of spindles with the fiber planes with MP tilts  $\leq 10^\circ$  (Fig. 3c(i)). We note that the reduced MP tilt is due to stronger CS–RF attraction at low  $h_f$  ( $<1\ \mu\text{m}$ ) that counters the CS–CRTX attractive forces from the remaining cortex, thus aligning the spindle parallel to the fiber plane (Fig. S17a). However, the absence of cortical deformation might allow MP translation ( $h_f > 1\ \mu\text{m}$ ), leading to a certain fraction of cases displaying tilted MPs (Fig. 3c(i), inset). At  $h_f > 1\ \mu\text{m}$ , signifying the positioning of MP in one of the cellular lobes; the observed high MP tilt is due to one CS pole positioned far from RF regions driven by the CS–CRTX attraction, while the other pole remains close to RFs on the opposite cell side influenced by the CS–RF attractive

forces (Fig. S17b). Next, we examined the role of cortical deformations without and with the presence of RFs. We reasoned that high cortical deformation near the fiber plane ( $h_f \leq 1\ \mu\text{m}$ ) could physically limit the MP's translation in one of the cellular lobes, thus significantly reducing the tilting. We discovered that without RFs (i.e. with uniform distribution of cortical cues for CS–CRTX interactions), pinching was inadequate for aligning the spindle with the fiber plane, resulting in a broad distribution of MP tilt angles (Fig. 3c(ii)). Strikingly, combining the effects of cortical deformation ( $C = 4\ \mu\text{m}$ ) and RFs in the simulations resulted in a significant rise ( $\sim 33\%$ ) in the proportion of cells with low MP tilts ( $\leq 10^\circ$ ; Fig. 3c(iii)) compared with RFs alone (Fig. 3c(i)). Our simulations at different values of cortical deformation further elucidate the cooperativity of RFs and cortical deformations under two conditions ( $h_f < 1\ \mu\text{m}$  and  $h_f > 1\ \mu\text{m}$ ; Fig. S15). At  $h_f < 1\ \mu\text{m}$ , we observed a decrease in MP tilt angle with increasing cortical deformation, while at  $h_f > 1\ \mu\text{m}$ , we observed high tilt angles independent of cortical deformations.

Overall, we show that the MP tilt is sensitive to the positioning of MP relative to the fiber plane. MP centroid away from the fiber plane exhibits high MP tilt due to the reduced influence of RFs. MP centroid close to the fiber plane predominantly exhibits low MP tilts due to the influence of RFs as the primary mechanical cues for spindle alignment. Cortical deformation, which physically interacts with the MP, further enhances the proportion of cells displaying low MP tilt angles.

## Discussion

We report how mechanical ECM confinement impacts the positioning and orientation of mitotic spindles. We generate a repeatable system of cells undergoing division using aligned nanofiber networks of interfiber spacing  $12\ \mu\text{m}$ , allowing the mitotic cells to confine between the external fibers at varying levels. The fibers are suspended and flexible, which allows the natural and complete rounding of cells. We observed that mitotic HeLa cells, having diameters much larger than the interfiber spacing, experience significant confinement effects, with almost 55% of cells entrapped between these fibers while rounding up for mitosis. In denser ECM environments with closer fiber spacing (50), we expect to get a mitotic response of cells attached to three or more fibers, with cells sitting atop fibers (9). Thus, our approach establishes a method to study the mitotic outcomes under confinement as expected in sparse fibrous in vivo environments of loose connective and interstitial tissue with interfiber spacing ranging from a few to  $20\ \mu\text{m}$  (18–24). Our experimental fiber arrangement and spacing closely resemble recent in vivo observations of aligned collagen fibers interacting with breast cancer cells (25). In the intravital images and time-lapse movies, cells were observed migrating along aligned collagen fibers, deforming the fibers with their protrusive tips (25). A closer look at these images suggests that a few roundish cells remain confined between the fiber doublets. In our setup, cells rounding up during mitosis deform the fiber networks while being held in position by RFs that connect the cell cortex to the adhesion sites. We find that the extent of confinement pattern RFs on the cortex and the deformed ECM fibers apply a restorative compression to cause a local deformation in the cell cortex and, consequently, in the MP. Our study reveals distinct RF patterns emerge as a function of the positioning of the cell body with respect to the fiber plane. In the unconfined state, the fibers are positioned at the bottom of the cell body; thus, the RFs start from below and terminate toward the middle of the cell body, forming a triangular pattern on the cell cortex. Under high confinement,

the fiber plane is situated mid-body, thus creating a band-like RF pattern. By combining quantitative microscopy and computational modeling, we mechanistically interrogate the combined effects of confinement-driven RF patterning and cortical deformation in regulating the MP positioning, orientation, and mitotic duration.

While mechanical confinement and cell–ECM/cell–cell connections have been individually shown to influence mitotic spindle orientation, their combined effects remain poorly understood. Disruption of RF-mediated connections in unconfined cells through pharmacological treatment or laser ablation results in mitotic spindle misalignment (1, 6, 7). Using a vertical microcantilever array, Sorce et al. demonstrated that confined cells with insufficient rounding force (impaired actin cytoskeleton) can undergo large spindle rotations ( $\sim 70^\circ$ ) (44). In vivo, confined mitotic cells behave similarly, with an almost orthogonal reorientation of the mitotic spindle upon loss of actin cortical tension (51). At the cellular level, two major forces dominate: (i) the outward rounding forces at the start of cell division caused by a multifold increase in the cortical tension (52) and the intracellular hydrostatic pressure (5) and (ii) the pulling forces exerted on the rounded cell body, either from the neighboring ECM (actin-rich RFs) (1, 2, 9, 53) or neighboring cells (cell–cell cadherin-based connections) in a tissue (53–55). Mitotic rounding forces counteract the externally imposed mechanical confinement from surrounding ECM or cells and have been previously measured in vitro via AFM cantilevers and vertical cantilever arrays (4, 5, 56). Contractile forces existing within RFs have been characterized via optical tweezers. Our deformable nanonets allow us to quantify the mitotic rounding forces while indirectly measuring the forces within each RF. A caveat in our force measurement is that forces are calculated from the top view; thus, we cannot relate the force values with the extent of confinement. However, the mitotic force calculation of 12–14 nN is similar to the  $\sim 15$  nN peak force for HeLa cells reported using the vertical cantilever assay (44). Furthermore, our estimate of RF tension ( $\sim 214$  pN) from cells not completely rounded agrees with previously reported values using optical tweezers (250 pN) (1).

We observed MP tilting and positioning depending on the extent of confinement. To gain a mechanistic understanding of these outcomes, we utilized our computational model, encompassing various MT-dependent forces regulated by internal and external factors involved in mitotic spindle organization. Numerous studies have shown that a cortically localized protein complex composed of Gai, LGN, and NuMA facilitates the recruitment of the MT minus-end-directed dynein–dynactin complex to the cell cortex, exerting pulling forces on the astral MTs extending from spindle poles (57, 58). External factors of RFs and confinement can significantly alter spindle orientation by causing a reorganization of the internal molecular components and enriching them in the cortical region attached to RFs (6–8, 38, 53) or the intercellular junctions (33, 53, 54, 59). In addition to Gai/LGN/NuMA, other cortical mechanosensory proteins, such as integrins, FAK, Src, p130Cas, caveolin-1, and MISP, have been found to enrich near the cortex region connected to RFs, exerting a significantly stronger pull on the CSs via the astral MTs than the rest of the cell cortex (6–9, 38). Our simulations account for experimentally observed cortical cues in RF-covered and RF-free cortical regions through CS–RF and CS–CRTX attractive forces, respectively (Fig. 4). Notably, in the unconfined cells (low ECM confinement), positioning the rounded cell body at or above the fiber plane results in a triangular pattern of RFs that cover a large area on the cell cortex spanning from the fiber plane (sites of adhesions) to the equatorial plane of the cell body. Thus, we expect that a larger

RF coverage area will attract evolving CS clusters on opposite cell halves toward the corresponding RF regions with enhanced CS–RF attractive forces, which will subdue the effect of the CS–CRTX attraction from the remaining cortex. The larger RF regions, in turn, align the mitotic spindle parallel to the equatorial plane (analogously to the external fiber plane), yielding smaller MP tilts (Fig. 4). On the other hand, in confined cells (high ECM confinement), the band-like arrangement of RFs at or near the equatorial plane with reduced RF coverage results in a relatively weaker influence of the CS–RF forces while enhancing the net CS–CRTX attraction. These competing forces acting on the CSs lead to more MPs acquiring a greater tilt angle than the unconfined cells (Fig. S10). Furthermore, our computational model reveals a surprising role of the triangular shape of RF patterns in yielding smaller MP tilt angles at low confinement. Within a diverse array of simulated RF patterns on the spherical cortex, the only configurations matching the experimentally observed trend of MP tilt are those with triangular RF patterns. Conversely, deviations from triangular RF patterns, such as rectangular RF spots or compact band-like patterns extending from the fiber plane to the cell equator at low ECM confinement, lead to MP tilting, inconsistent with experiments (Table SI, Cases 1–3).

In addition to the small RF coverage due to band-like RF patterning, cells at high confinement exhibit significant cortical deformation caused by external fibers. The mechanical imbalance between the outward mitotic rounding forces deflecting the fibers and the inward compression from these deflected fibers, possibly caused by the variations in cell size, cortex stiffness, and heterogeneous fluctuations in external fibers during cell rounding, results in varying levels of cortical deformation at high confinement. We investigated whether such deformation in the cell cortex can subdue the effect of low RF coverage that contributes to the tilting of the MP. Indeed, our experiments and computational studies show that increased cortical deformation, leading to localized MP deformation, correlates inversely with MP tilt angles. Deformation may constrain the MPs to be physically limited in movement, which works in tandem with RF cues to reduce the MP tilt by outweighing the CS–CRTX attractions from the remaining cortex, which are responsible for spindle misalignment (tilted MP; Fig. 4). To determine the combined ability of cortical deformation and RF cues, we simulated our model under three conditions: cortical deformation only, RF cues only, and a combination of both these cues. The MP tilt angles are random under cortical deformation alone (without RFs), consistent with previous findings in cells cultured on poly-L-lysine that cannot establish RFs and, thus, display random orientations of the mitotic spindle (6, 7, 60). However, the sole presence of RFs in the model caused more cells to have low MP tilts. Combining both cues (cortical deformation and RFs) substantially increased MPs with low tilt occurrences. Altogether, our study reveals a possible correlation between the positioning of MPs relative to the fiber plane and the resulting MP tilt angles (Fig. 4). MPs located close to the fiber plane predominantly exhibit reduced tilt angles due to the influence of CS–RF attraction and physical constraints on MPs due to pinching from the external fibers. On the other hand, MPs positioned further away from the fiber plane tend to have higher MP tilt angles due to dominant CS–CRTX attractive forces from the remaining cell cortex.

Interestingly, cells under high ECM confinement correlate with faster progression through mitosis. It is well established that the formation of stable, amphitelic KT–microtubule attachments triggers spindle assembly checkpoint silencing and mitotic exit (61, 62). A key question raised by our studies is: Why do such

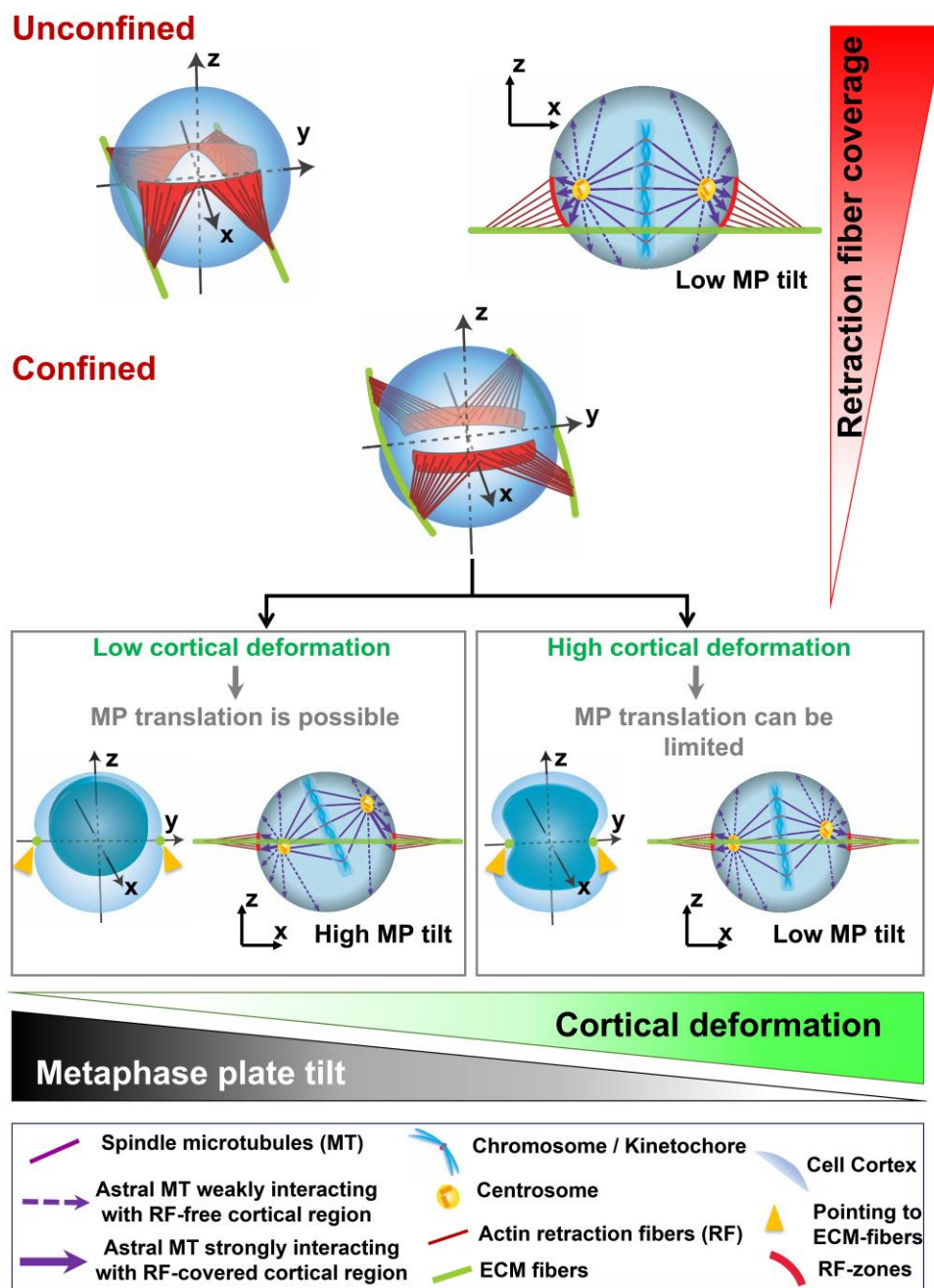


**Fig. 4.** A schematic representation of model outcomes outlining the role of RF organization and cortical deformation regulating MP orientation. Front ( $xz$ ) schematics of the cell show MP tilt and corresponding spindle orientation. Unconfined cells have triangular RF coverage that gives rise to low MP tilts. In contrast, confined cells have reduced RF coverage due to band-like patterning. Under confinement, external fibers can pinch the cell cortex, leading to local deformation of the MP. Low cortical deformation, with no MP deformation, generally allows for translation of the MP in one of the cellular lobes, resulting in a high MP tilt prompted by CS–CRTX attraction. In contrast, high cortical deformation accompanied by localized MP deformation may impose physical constraints on MP movement, reducing the overall MP tilt.

attachments form more quickly under ECM confinement? One possibility is that, in confined cells, CSs tend to position on opposite sides of the cell near the mid-cortical level, influenced by RFs on the equatorial surface. In contrast, in unconfined cells, where RFs are distributed over a broader region below the mid-cortical level, CSs are positioned significantly below the mid-cortical level. This centrosomal arrangement under low ECM confinement may delay the attachment of microtubules to KTs on CHs located in the hemisphere lacking CSs because microtubules must sample a larger area as they search for CHs/KTs. Delayed contact may reduce the activity of motor proteins, such as CENP-E (kinesin-7), which

facilitate lateral CH transport toward the spindle mid-plane upon microtubule–KT interaction, promoting CH alignment (63–65). Consequently, it might delay the formation of stable amphitelic attachments, leading to longer mitotic transit times.

Our results on cell division under ECM confinement reveal fundamental insights into how external mechanical signals influence the organization of the MP and, subsequently, the dynamics of resulting daughter cells. Time-lapse movies from the top view of cells in our study reveal that spindles with low MP tilt facilitate the in-plane spreading of daughter cells along external fibers (Movie S4). In contrast, high MP tilt can cause one daughter cell

to stay on the original fiber doublet and the other to move to a neighboring doublet (Movie S5). This observation could have broader implications for tissue organization. Low MP tilt supports in-plane division, crucial for epithelial integrity and tissue elongation. In contrast, high MP tilt can disrupt this integrity by causing one daughter cell to detach, potentially leading to tissue stratification or promoting physiological disorders (28, 33–36). The flexibility of confining ECM fibers in our study plays a crucial role in facilitating the natural rounding of mitotic cells by outward deflection of the external fibers, thus promoting the timely progression of mitosis. In contrast, previous studies involving cells confined within microchannels (66, 67), AFM cantilevers (4), inside dense gels (14, 40), or others (68) show improper mitotic rounding under high confinement, resulting in spindle organization defects and impaired mitotic progression. These observations emphasize the crucial influence of the geometry and flexibility of fibrous ECM environments in shaping mitotic spindle dynamics and ensuring mitotic progression. Our study disambiguates the contributions from RFs and local deformations in the MP. It shows that the positioning of MP and confinement-driven patterning of RFs on the cortex are critical determinants of mitotic spindle angular positioning within the rounded cell body. Moreover, our findings open exciting opportunities to explore confinement-based outcomes in multiple scenarios, including stratification, sprouting, maintenance, growth, and tumorigenicity (53). However, we acknowledge certain limitations in assessing the dynamic behavior of the MP tilt. While our work demonstrates the influence of confinement and cortical deformations on MP organization, the lack of time-lapse volumetric imaging limits our ability to capture real-time fluctuations of the MP tilt in three dimensions and the full kinetics of cell rounding and confinement between fibers. Advanced imaging techniques would provide deeper insights into these temporal dynamics. Mitotic spindle organization and cell division are complex biological processes involving many components and processes; a simple explanation of this complexity through a reductionist approach, whether experimental or computational, remains challenging. The qualitative agreement between simulations and experiments demonstrates that our model captures essential interactions and significantly advances mitotic biology. Overall, we identify a new role of fibrous ECM in confinement mitotic biology and shed light on how cells might undergo mitosis with angularly misplaced mitotic spindles *in vivo*.

## Materials and methods

### Generation of nanofiber networks

Aligned and suspended fiber networks were generated from solutions of polystyrene (Scientific Polymer Products, Ontario, NY, United States of America) dissolved in xylene (X5-500; Thermo Fisher Scientific, Waltham, MA, United States of America), using our previously reported nonelectrospinning Spinneret-based Tunable Engineered Parameters technique (69–71). Force-sensing 250 nm fibers were generated from 7 wt% solutions of polystyrene (MW: 2,000,000 g/mol) in xylene and deposited with a 12- $\mu$ m interfiber spacing on top of large diameter (2  $\mu$ m) support fibers prepared from 5 wt% solutions of polystyrene (MW: 15,000,000 g/mol; Agilent Technologies) dissolved in xylene. Fiber networks were bonded at intersection points utilizing solvent vapor in a custom fusing chamber. The elastic modulus of fibers (~1–3 GPa) (72) closely matches the reported values of collagen fibers (~2–5 GPa) (73–75). The chosen diameter (250 nm) falls within a broad range of ECM fiber diameters (22, 76, 77).

The lengths of the fiber networks can also span hundreds of micrometers. Thus, the fiber networks used in our system represent ECM dimensions and mechanical properties.

### Cell culturing and mitotic synchronization

HeLa cells expressing histone H2B GFP were cultured in Dulbecco's modified Eagle's medium (Invitrogen, Carlsbad, CA, United States of America) supplemented with 10% fetal bovine serum (Gibco, Thermo Fisher Scientific) in T25 flasks (Corning, Corning, NY, United States of America) and maintained at 37 °C and 5% CO<sub>2</sub> in a humidified incubator. Nanofiber networks were sterilized with 70% ethanol and functionalized with 4  $\mu$ g/mL of rhodamine-conjugated fibronectin (Cytoskeleton Inc.) in PBS for 1 h to enable cell–fiber attachment.

Cell division synchronization was performed by treating cells with 9  $\mu$ M of the Cdk1 inhibitor RO-3306 for 20 h (9). Cells were subsequently released for the division after five times wash with complete culture media.

### Time-lapse imaging of mitotic cells

Cells cultured on fibers were imaged every 5 min with a 20 $\times$  0.8 NA objective in a wide-field microscope (Zeiss AxioObserver Z1) equipped with a FITC filter set for GFP fluorescence. Experiments were performed under incubation conditions of 37 °C and 5% CO<sub>2</sub> (Zeiss, Oberkochen, Germany). Mitosis duration was estimated from the time-lapse imaging and was taken from the start of the nuclear envelope breakdown (NEBD) to the initiation of telophase.

### Immunofluorescent staining and imaging

Cells synchronized with the Cdk1 inhibitor RO-3306 were released with a drug washout and monitored for mitotic entry. Cells were fixed with 4% paraformaldehyde (15 min) after ~1 h after drug washout, where the maximal number of cells were observed (by visual inspection) to be in metaphase. Fixed cells were permeabilized in 0.1% Triton X-100 solution for 15 min and blocked with 5% goat serum (Invitrogen, Grand Island, NY, United States of America) for 45 min. Primary antibodies were diluted in an antibody dilution buffer consisting of PBS with 1% bovine serum albumin and Triton-X 100 and stored overnight at 4 °C. Primary antibodies include anti-beta tubulin (1:500, mouse monoclonal, 28 33; Invitrogen) and anti-Hec1 (1:1,000, human monoclonal) for labeling microtubules and KTs, respectively. Secondary antibodies diluted in antibody dilution buffer were added along with the conjugated Phalloidin-TRITC (Santa Cruz Biotechnology) or Alexa Fluor 647 Phalloidin (1:40–1:80; Invitrogen) and stored in a dark place for 45 min. Secondary antibodies include donkey anti-human IgG Alexa Fluor 555 (1:600) and goat anti-mouse IgG Alexa Fluor 405 (1:500; Invitrogen). Confocal microscopy was performed using a laser scanning confocal microscope (LSM 880; Carl Zeiss Inc.) with optimal imaging settings and z-slice thicknesses ranging from 0.36 to 0.5  $\mu$ m.

### Analysis of cell parameters

Confocal z-stacks of fluorescently labeled rounded mitotic cells were visualized in the Zeiss Zen software or ImageJ. The Ortho function in Zen software was utilized to generate the top view (xy) and the cross-sectional front (xz) and side (yz) views. Mitotic cell height and aspect ratio were computed from the cross-sectional yz side views of cells by manual outlining in ImageJ. The cortical perimeter of the cell was estimated from the xz front view of cells.

## MP orientation analysis

The MP tilt was most evident from the front view of the confocal z-stacks; thus, the xz front views were used to calculate the MP tilt. Measurements were taken with respect to the reference line orthogonal to the plane of the fibers (Fig. 2a).

## RF analysis

Z-stacks of phalloidin-stained cells were used to quantify the 3D organization of RFs. Mainly, xz front views are generated, and the arc length covered by RFs on either side of the cell (Fig. 2b) is measured in ImageJ using the segment line tool. The RF coverage metric is a binary metric that describes the extent of the cell surface covered with RFs.

## Quantification of cell forces

Deflections of nanofibers during interphase (contractile cell state, inward fiber deflections) and cell rounding (expansive rounded state, outward fiber deflections) were converted to force (nN) values using our previously reported Nanonet Force Microscopy (41, 42, 72). Briefly, fibers are modeled as Euler–Bernoulli beams with fixed boundary conditions and subjected to point loads at the cell–fiber contact regions (Appendix I in Supplementary Material).

## Statistical analysis

Statistical analysis was performed in GraphPad Prism (GraphPad Software, La Jolla, CA, United States of America) software. Statistical comparison among multiple groups was performed using one-way ANOVA and Tukey's honestly significant difference test. Pairwise statistical comparisons were performed using Student's t-test. Error bars in scatter data plots indicate SD. \*, \*\*, \*\*\*, and \*\*\*\* represent  $P < 0.05$ , 0.01, 0.001, and 0.0001, respectively.

## Computational modeling

Typically, the HeLa cell lines we have used in the experiments can show multicentrosomal characteristics (9, 78). Here, we focused only on the bipolar regime of the metaphase spindle. Accordingly, we designed our numerical protocols with several CSs and analyzed the spindle orientations only for bipolar spindles (Fig. S18). The choice of the parameter space ensures a majority of bipolar spindles with eight CSs (9, 45). However, choosing eight CSs is arbitrary and applicable to any number (45). To maintain the bipolar majority, each CS exerts attractive forces on other CSs, KTs, and cell membranes while repelling the CH arms. These forces arise from the interaction of CS-nucleated microtubules with another CS, possibly via dynein or kinesin-14, microtubules connecting CSs to KTs and cell membranes via dynein or pushing the chromosomal arms via chromokinesins (such as kinesin-10 and kinesin-4) (47, 48, 79–81). Considering such attractive and repulsive force combinations is consistent with other models of multicentrosomal clustering into bipolar spindles (13, 46, 82). We carried out our simulations with CSs and CHs represented as particle-like objects positioned at nodes of a cubic lattice confined within a cellular volume. The large lattice structure growing beyond the cell membrane allows the discretization of the cell surface into a finite number of roughly equidistant nodes, similar to the grid size inside the cell. The surface nodes are divided into regions devoid of or coupled to RFs. Notably, the surface regions covered by RFs interact more strongly with CSs through attractive forces than the remaining surface regions (9). Using a Monte Carlo simulation, we determine the temporal evolution of CSs and CHs within the cell volume. The potential energies from pairwise

interaction forces among CSs, CHs, and the cell membrane are estimated. Achieving the minimum energy ensured a mechanical equilibrium configuration of the spindle. The subsequent equilibrium snapshots are chosen to characterize spindle dynamics and measure chromosomal tilt. The model was calibrated using varying values of confinement ( $h/H$ ) and cortex deformation ( $C$ ), which were used as inputs for the computational simulations. The computational model is prepared with cells deformed around the mid-cortex for  $h/H \sim 0.5$ , achieving geometric similarity to the experiment. For different levels of cortical deformations, the model predicts the MP position ( $h_f$ ) and tilt. For more detailed information on the simulation methods, please refer to Appendix II in Supplementary Material.

## Acknowledgments

A.S.N. acknowledges the Institute of Critical Technologies and Science (ICTAS) and Macromolecules Innovative Institute (MII) at Virginia Tech for supporting this study. A.S. and R.P. acknowledge Indian Association for the Cultivation of Science (IACS), Kolkata, for funding support and providing computational facilities.

## Supplementary Material

Supplementary material is available at PNAS Nexus online.

## Funding

A.S.N. acknowledges partial funding support from the National Science Foundation (NSF, grant nos.: 2107332 and 2119949) and the National Institute of Health (NHLBI award #HL162822). J.G.D. acknowledges funding support from the NIH (R35GM130365).

## Author Contributions

A.S.N. conceived the study. A.S., A.J., A.A., N.S.G., J.G.D., R.P., and A.S.N. designed the research. A.J., A.A., and J.W. performed the time-lapse imaging experiments. A.J. and A.A. performed the confocal imaging experiments. A.J., A.A., J.W., R.K., and A.S.N. implemented the nanonet force microscopy. A.S. and R.P. developed the computational models and performed simulations. J.G.D. and A.S.N. contributed the new reagents/analytic tools. A.S., A.J., A.A., N.S.G., J.G.D., R.P., and A.S.N. analyzed the data. A.S., A.J., A.A., R.P., and A.S.N. wrote the paper. All authors contributed to editing and revisions of the paper.

## Preprints

This manuscript was posted on a preprint at <https://doi.org/10.1101/2024.04.12.589246>.

## Data Availability

All data are included in the manuscript and Supplementary Material.

## References

- 1 Fink J, et al. 2011. External forces control mitotic spindle positioning. *Nat Cell Biol.* 13:771–778.
- 2 Théry M, et al. 2005. The extracellular matrix guides the orientation of the cell division axis. *Nat Cell Biol.* 7:947–953.

- 3 Théry M, Jiménez-Dalmaroni A, Racine V, Bornens M, Jülicher F. 2007. Experimental and theoretical study of mitotic spindle orientation. *Nature*. 447:493–496.
- 4 Cattin CJ, et al. 2015. Mechanical control of mitotic progression in single animal cells. *Proc Natl Acad Sci U S A*. 112:11258–11263.
- 5 Stewart MP, et al. 2011. Hydrostatic pressure and the actomyosin cortex drive mitotic cell rounding. *Nature*. 469:226–230.
- 6 Petridou NI, Skourides PA. 2016. A ligand-independent integrin  $\beta 1$  mechanosensory complex guides spindle orientation. *Nat Commun*. 7:10899.
- 7 Petridou NI, Skourides PA. 2014. FAK transduces extracellular forces that orient the mitotic spindle and control tissue morphogenesis. *Nat Commun*. 5:5240.
- 8 Maier B, Kirsch M, Anderhub S, Zentgraf H, Krämer A. 2013. The novel actin/focal adhesion-associated protein MISP is involved in mitotic spindle positioning in human cells. *Cell Cycle*. 12:1457–1471.
- 9 Jana A, et al. 2023. Mitotic outcomes and errors in fibrous environments. *Proc Natl Acad Sci U S A*. 120:e2120536120.
- 10 Matthews HK, et al. 2020. Oncogenic signaling alters cell shape and mechanics to facilitate cell division under confinement. *Dev Cell*. 52:563–573.e3.
- 11 Devany J, Falk MJ, Holt LJ, Murugan A, Gardel ML. 2023. Epithelial tissue confinement inhibits cell growth and leads to volume-reducing divisions. *Dev Cell*. 58:1462–1476.e8.
- 12 Fernandez P, et al. 2011. Mitotic spindle orients perpendicular to the forces imposed by dynamic shear. *PLoS One*. 6:e28965.
- 13 Cheng L, Li J, Sun H, Jiang H. 2023. Appropriate mechanical confinement inhibits multipolar cell division via pole-cortex interaction. *Phys Rev X*. 13:011036.
- 14 Lancaster OM, et al. 2013. Mitotic rounding alters cell geometry to ensure efficient bipolar spindle formation. *Dev Cell*. 25:270–283.
- 15 Nam S, et al. 2019. Cell cycle progression in confining microenvironments is regulated by a growth-responsive TRPV4-PI3K/Akt-p27Kip1 signaling axis. *Sci Adv*. 5:eaaw6171.
- 16 He L, et al. 2015. Local 3D matrix confinement determines division axis through cell shape. *Oncotarget*. 7:6994–7011.
- 17 Cadart C, Zlotek-Zlotkiewicz E, Le Berre M, Piel M, Matthews HK. 2014. Exploring the function of cell shape and size during mitosis. *Dev Cell*. 29:159–169.
- 18 Ushiki T. 2002. Collagen fibers, reticular fibers and elastic fibers. A comprehensive understanding from a morphological viewpoint. *Arch Histol Cytol*. 65:109–126.
- 19 Fernández M, et al. 2002. Small-angle x-ray scattering studies of human breast tissue samples. *Phys Med Biol*. 47:577–592.
- 20 Weigelin B, Bakker G-J, Friedl P. 2012. Intravital third harmonic generation microscopy of collective melanoma cell invasion: Principles of interface guidance and microvesicle dynamics. *IntraVital*. 1:32–43.
- 21 Conklin MW, et al. 2011. Aligned collagen is a prognostic signature for survival in human breast carcinoma. *Am J Pathol*. 178:1221–1232.
- 22 Gritsenko PG, Ilna O, Friedl P. 2012. Interstitial guidance of cancer invasion. *J Pathol*. 226:185–199.
- 23 Friedl P, Wolf K. 2009. Proteolytic interstitial cell migration: a five-step process. *Cancer Metastasis Rev*. 28:129–135.
- 24 Wolf K, et al. 2009. Collagen-based cell migration models in vitro and in vivo. *Semin Cell Dev Biol*. 20:931–941.
- 25 Szulczewski JM, et al. 2021. Directional cues in the tumor microenvironment due to cell contraction against aligned collagen fibers. *Acta Biomater*. 129:96–109.
- 26 Morin X, Bellaïche Y. 2011. Mitotic spindle orientation in asymmetric and symmetric cell divisions during animal development. *Dev Cell*. 21:102–119.
- 27 Williams SE, Fuchs E. 2013. Oriented divisions, fate decisions. *Curr Opin Cell Biol*. 25:749–758.
- 28 Ragkousi K, Gibson MC. 2014. Cell division and the maintenance of epithelial order. *J Cell Biol*. 207:181–188.
- 29 Gillies TE, Cabernard C. 2011. Cell division orientation in animals. *Curr Biol*. 21:R599–R609.
- 30 Noatynska A, Gotta M, Meraldi P. 2012. Mitotic spindle (DIS)orientation and DISease: cause or consequence? *J Cell Biol*. 199:1025–1035.
- 31 Pease JC, Tirnauer JS. 2011. Mitotic spindle misorientation in cancer—out of alignment and into the fire. *J Cell Sci*. 124:1007–1016.
- 32 Tan CH, et al. 2015. The equatorial position of the metaphase plate ensures symmetric cell divisions. *Elife*. 4:e05124.
- 33 Lisica A, et al. 2022. Tension at intercellular junctions is necessary for accurate orientation of cell division in the epithelium plane. *Proc Natl Acad Sci U S A*. 119:e2201600119.
- 34 van Leen EV, di Pietro F, Bellaïche Y. 2020. Oriented cell divisions in epithelia: from force generation to force anisotropy by tension, shape and vertices. *Curr Opin Cell Biol*. 62:9–16.
- 35 Lechler T, Fuchs E. 2005. Asymmetric cell divisions promote stratification and differentiation of mammalian skin. *Nature*. 437:275–280.
- 36 Huebner RJ, Lechler T, Ewald AJ. 2014. Developmental stratification of the mammary epithelium occurs through symmetry-breaking vertical divisions of apically positioned luminal cells. *Development*. 141:1085–1094.
- 37 Nakajima YI. 2018. Mitotic spindle orientation in epithelial homeostasis and plasticity. *J Biochem*. 164:277–284.
- 38 Matsumura S, et al. 2016. Interphase adhesion geometry is transmitted to an internal regulator for spindle orientation via caveolin-1. *Nat Commun*. 7:ncomms11858.
- 39 Campinho P, et al. 2013. Tension-oriented cell divisions limit anisotropic tissue tension in epithelial spreading during zebrafish epiboly. *Nat Cell Biol*. 15:1405–1414.
- 40 Nam S, Chaudhuri O. 2018. Mitotic cells generate protrusive extracellular forces to divide in three-dimensional microenvironments. *Nat Phys*. 14:621–628.
- 41 Jana A, et al. 2022. Sculpting rupture-free nuclear shapes in fibrous environments. *Adv Sci*. 9:e2203011.
- 42 Mukherjee A, et al. 2023. Actin filaments couple the protrusive tips to the nucleus through the I-BAR domain protein IRSp53 during the migration of cells on 1D fibers. *Adv Sci*. 10:e2207368.
- 43 Padhi A, et al. 2020. Force-exerting perpendicular lateral protrusions in fibroblastic cell contraction. *Commun Biol*. 3:390.
- 44 Sorce B, et al. 2015. Mitotic cells contract actomyosin cortex and generate pressure to round against or escape epithelial confinement. *Nat Commun*. 6:8872.
- 45 Chatterjee S, et al. 2020. Mechanics of multicentrosomal clustering in bipolar mitotic spindles. *Biophys J*. 119:434–447.
- 46 Miles CE, Zhu J, Mogilner A. 2022. Mechanical torque promotes bipolarity of the mitotic spindle through multi-centrosomal clustering. *Bull Math Biol*. 84:29.
- 47 Ferenz NP, Paul R, Fagerstrom C, Mogilner A, Wadsworth P. 2009. Dynein antagonizes Eg5 by crosslinking and sliding antiparallel microtubules. *Curr Biol*. 19:1833–1838.
- 48 Mogilner A, Wollman R, Civelekoglu-Scholey G, Scholey J. 2006. Modeling mitosis. *Trends Cell Biol*. 16:88–96.
- 49 Dietz R. 1972. Anaphase behaviour of inversions in living crane-fly spermatocytes. *Chromosom Today*. 3:70–85.
- 50 Sun B. 2021. The mechanics of fibrillar collagen extracellular matrix. *Cell Reports Phys Sci*. 2:100515.

- 51 Nakajima Y, Meyer EJ, Kroesen A, McKinney SA, Gibson MC. 2013. Epithelial junctions maintain tissue architecture by directing planar spindle orientation. *Nature*. 500(7462):359–362.
- 52 Chugh P, et al. 2017. Actin cortex architecture regulates cell surface tension. *Nat Cell Biol*. 19:689–697.
- 53 Lechler T, Mapelli M. 2021. Spindle positioning and its impact on vertebrate tissue architecture and cell fate. *Nat Rev Mol Cell Biol*. 22:691–708.
- 54 Hart KC, et al. 2017. E-cadherin and LGN align epithelial cell divisions with tissue tension independently of cell shape. *Proc Natl Acad Sci U S A*. 114:E5845–E5853.
- 55 den Elzen N, BATTERY CV, Maddugoda MP, Ren G, Yap AS. 2009. Cadherin adhesion receptors orient the mitotic spindle during symmetric cell division in mammalian epithelia. *Mol Biol Cell*. 20:3740–3750.
- 56 Müller DJ, Dufrêne YF. 2011. Force nanoscopy of living cells. *Curr Biol*. 21:R212–R216.
- 57 Nguyen-Ngoc T, Afshar K, Gönczy P. 2007. Coupling of cortical dynein and G alpha proteins mediates spindle positioning in *Caenorhabditis elegans*. *Nat Cell Biol*. 9:1294–1302.
- 58 Kotak S, Busso C, Gönczy P. 2012. Cortical dynein is critical for proper spindle positioning in human cells. *J Cell Biol*. 199:97–110.
- 59 Zheng Z, et al. 2010. LGN regulates mitotic spindle orientation during epithelial morphogenesis. *J Cell Biol*. 189:275–288.
- 60 Bershadsky A, Chausovsky A, Becker E, Lyubimova A, Geiger B. 1996. Involvement of microtubules in the control of adhesion-dependent signal transduction. *Curr Biol*. 6:1279–1289.
- 61 Musacchio A, Desai A. 2017. A molecular view of kinetochore assembly and function. *Biology (Basel)*. 6:5.
- 62 Lara-Gonzalez P, Pines J, Desai A. 2021. Spindle assembly checkpoint activation and silencing at kinetochores. *Semin Cell Dev Biol*. 117:86–98.
- 63 Wood KW, Sakowicz R, Goldstein LS, Cleveland DW. 1997. CENP-E is a plus end-directed kinetochore motor required for metaphase chromosome alignment. *Cell*. 91:357–366.
- 64 Heald R, Khodjakov A. 2015. Thirty years of search and capture: The complex simplicity of mitotic spindle assembly. *J Cell Biol*. 211:1103–1111.
- 65 Lakshmi RB, et al. 2024. CKAP5 stabilizes CENP-E at kinetochores by regulating microtubule-chromosome attachments. *EMBO Rep*. 25(4):1909–1935.
- 66 Cadart C, et al. 2018. Size control in mammalian cells involves modulation of both growth rate and cell cycle duration. *Nat Commun*. 9:3275.
- 67 Xi W, et al. 2016. Molecular insights into division of single human cancer cells in on-chip transparent microtubes. *ACS Nano*. 10:5835–5846.
- 68 Tse HTK, Weaver WMC, Di Carlo D. 2012. Increased asymmetric and multi-daughter cell division in mechanically confined microenvironments. *PLoS One*. 7:e38986.
- 69 Nain AS, Sitti M, Jacobson A, Kowalewski T, Amon C. 2009. Dry spinning based spinneret based tunable engineered parameters (STEP) technique for controlled and aligned deposition of polymeric nanofibers. *Macromol Rapid Commun*. 30:1406–1412.
- 70 Wang J, Nain AS. 2014. Suspended micro/nanofiber hierarchical biological scaffolds fabricated using non-electrospinning STEP technique. *Langmuir*. 30:13641–13649.
- 71 Nain AS, Wang J. 2013. Polymeric nanofibers: isodiametric design space and methodology for depositing aligned nanofiber arrays in single and multiple layers. *Polym J*. 45:695–700.
- 72 Sheets K, Wang J, Zhao W, Kapania R, Nain AS. 2016. Nanonet force microscopy for measuring cell forces. *Biophys J*. 111:197–207.
- 73 Wenger MPE, Bozec L, Horton MA, Mesquida P. 2007. Mechanical properties of collagen fibrils. *Biophys J*. 93:1255–1263.
- 74 Silver FH, Freeman JW, Seehra GP. 2003. Collagen self-assembly and the development of tendon mechanical properties. *J Biomech*. 36:1529–1553.
- 75 Silver FH. *Mechanosensing and mechanochemical transduction in extracellular matrix: biological, chemical, engineering, and physiological aspects*. Vol. 24. Springer Science & Business Media, 2006.
- 76 Ottani V, et al. 1998. Collagen fibril arrangement and size distribution in monkey oral mucosa. *J Anat*. 192:321–328.
- 77 Padhi A, Nain AS. 2020. ECM in differentiation: a review of matrix structure, composition and mechanical properties. *Ann Biomed Eng*. 48:1071–1089.
- 78 Gergely F, Draviam VM, Raff JW. 2003. The ch-TOG/XMAP215 protein is essential for spindle pole organization in human somatic cells. *Genes Dev*. 17:336–341.
- 79 Chatterjee S, et al. 2021. Mechanics of microtubule organizing center clustering and spindle positioning in budding yeast *Cryptococcus neoformans*. *Phys Rev E*. 104:034402.
- 80 McNally FJ. 2013. Mechanisms of spindle positioning. *J Cell Biol*. 200:131–140.
- 81 Li Y, Yu W, Liang Y, Zhu X. 2007. Kinetochore dynein generates a poleward pulling force to facilitate congression and full chromosome alignment. *Cell Res*. 17:701–712.
- 82 Li X, Bloomfield M, Bridgeland A, Cimini D, Chen J. 2023. A fine balance among key biophysical factors is required for recovery of bipolar mitotic spindle from monopolar and multipolar abnormalities. *Mol Biol Cell*. 34:ar90.